

# Spectral properties of microcantilevers in viscous fluid

Matthew T. Clark

*Department of Mechanical Engineering, Virginia Polytechnic Institute and State University, Blacksburg, Virginia 24061, USA*

John E. Sader

*Department of Mathematics and Statistics, The University of Melbourne, Victoria 3010, Australia*

Jason P. Cleveland

*Asylum Research, 6310 Hollister Ave., Santa Barbara, California 93117, USA*

Mark R. Paul\*

*Department of Mechanical Engineering, Virginia Polytechnic Institute and State University, Blacksburg, Virginia 24061, USA*

(Received 28 December 2009; published 12 April 2010)

We explore analytically, numerically, and experimentally the spectral properties of the flexural vibrations of micron scale cantilevers in a viscous fluid that are driven externally or by Brownian motion. Although the physical origins of driven and thermal cantilever dynamics are quite different, we show that in each case the dynamics can be calculated deterministically using an impulse or step force, respectively. The stochastic dynamics of the cantilever are related to the removal of a step force by the fluctuation-dissipation theorem to yield the autocorrelation and noise spectral density of equilibrium fluctuations. The dynamics of a cantilever driven externally is related to an impulse in force by transfer function theory. Using this approach, we explore the differences between the driven and thermal spectra of microcantilevers. We find that higher order cantilever modes and the spatial distribution of the applied load for the external drive can be critical to the relationship between the thermal and driven spectra.

DOI: [10.1103/PhysRevE.81.046306](https://doi.org/10.1103/PhysRevE.81.046306)

PACS number(s): 47.61.Fg, 85.85.+j, 45.10.-b, 83.10.Mj

## I. INTRODUCTION

The dynamics of micron scale elastic cantilevers in viscous fluid are of broad scientific and technological interest [1,2]. For example, experiments using atomic force microscopy continue to make significant contributions in a wide variety of fields [3]. In practice, the cantilevers and their configurations can be quite complex. For example, cantilever geometries can be V-shaped [3], there are surrounding walls [4–6], there are arrays of cantilevers [7,8], and the cantilevers can be placed in vacuum with fluid filled channels embedded inside the cantilever [9,10].

Microcantilevers typically have rectangular or V-shaped planforms. Figure 1 shows two geometries that we will explore in detail. The cantilever dynamics can be generated by active or passive means. Common active drive techniques include magnetomotive, acoustic, and piezoelectric approaches [3]. We will also explore the dynamics of a V-shaped cantilever that is actuated using a recently developed magnetomotive drive approach [11] that is shown schematically in Fig. 1(b). A wire enters one leg of the V-shaped cantilever and leaves through the other. An electric current is passed through the wire while the cantilever is placed in a magnetic field resulting in a spatially varying Lorentz force that causes the cantilever to deflect. In a typical experiment, the magnetic field is varied sinusoidally in time and swept over a wide range of frequency, in order to measure the amplitude-frequency response of the cantilever. The time

variation in the angle of the cantilever tip is measured optically. On the other hand, passive actuation is the result of the thermal motion of matter and yields stochastic cantilever dynamics [12]. Despite the fact that the physical origin of the motion is seemingly quite different for active and passive actuation, we will show that in both cases the precise cantilever dynamics can be quantified in a unified manner using only deterministic calculations.

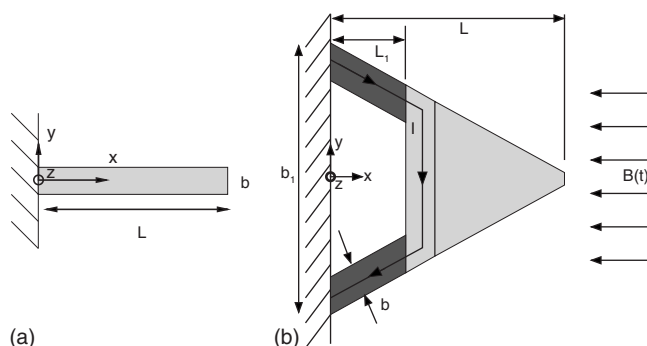


FIG. 1. Microcantilevers with rectangular and V-shaped planforms with coordinate directions  $(x, y, z)$ . (a) A rectangular cantilever of length  $L$ , width  $b$ , and thickness  $h$ . (b) A V-shaped cantilever of length  $L$ , arm length  $L_1$ , arm width  $b$ , and arm separation  $b_1$ . The V-shaped cantilever can be driven externally using magnetomotive actuation. The cantilever is placed in a sinusoidally varying magnetic field  $B(t)$  while a constant current  $I$  is applied, as shown, resulting in flexural displacements in the  $z$  direction due to the Lorentz force. Values for the material properties and geometry are given in Table I.

\*mrp@vt.edu

In an effort to keep the notation simple, we will refer to the spectral properties of the cantilever displacement or angle as the power spectrum  $P(\omega)$  or the noise spectral density  $G(\omega)$  when the cantilever is driven actively or thermally, respectively, where  $\omega$  is the frequency of oscillation. We note that the noise spectral density  $G(\omega)$  is a power spectral density whereas the power spectrum  $P(\omega)$  is the squared magnitude of the Fourier-transformed displacement/angle signal. The driven oscillations of the cantilever are found using basic ideas from transfer function theory by computing the cantilever response to a force impulse. The stochastic Brownian dynamics are determined from linear response theory and the fluctuation-dissipation theorem [13,14] by computing the cantilever response to the removal of a step force. The essence of our approach is captured by the Onsager regression hypothesis, which states that fluctuations at equilibrium are governed by the same laws in which a finite perturbation from equilibrium returns to equilibrium (cf. [15,16]). Although we consider only flexural oscillations the approach is quite general and can be applied to other modes of oscillation such as torsional or in-plane modes if desired. Using deterministic finite element numerical simulations for the precise geometries and conditions of interest allows us to compare directly with experimental results.

In this article, we provide a comprehensive and general approach capable of describing the deterministic and stochastic dynamics of micron and nanoscale cantilevers in a viscous fluid that is valid for a wide range of experimentally relevant conditions. Although the physical origins of the cantilever motion are quite different when the driving force is an external actuation or due to Brownian motion, we show that the cantilever dynamics can be understood using straight forward deterministic calculations. We develop this analytically and describe a numerical approach to implement these ideas to compare directly with experimental measurement. We find that contributions of higher flexural modes of vibration and the spatial variation in the driving force are essential to building a physical understanding of the relationship between thermal and externally driven spectra.

The paper is organized into three main sections. First, analytical expressions are developed for the power spectrum and noise spectral density valid in the limit of long and thin cantilevers undergoing small deflections. Next, a numerical approach is presented for calculating the noise and power spectra using simple deterministic calculations and we show that these results yield the exact analytical expressions given in Secs. II A and II B, respectively. We then present our findings and compare analytical, numerical, and experimental results to explore the driven and stochastic dynamics of a rectangular cantilever and a V-shaped cantilever in fluid. The ratio of the noise spectral density to the power spectrum is used to explore the spectral properties of the cantilevers.

## II. THEORY

We now consider the power spectrum and noise spectral density of a rectangular cantilever undergoing flexural oscillations in fluid. Our analytical description of a cantilever oscillating in fluid follows that of Sader [17]. The resulting

expressions are valid for long and thin cantilevers  $L \gg b \gg h$  and for small displacements [17] where  $L$  is the cantilever length,  $b$  is the cantilever width, and  $h$  is the cantilever thickness. In order to isolate the effects of higher flexural modes, we formulate the solution as an eigenfunction expansion of the cantilever mode shapes, in a manner similar to what is found in Refs. [18,19].

The equation governing the flexural oscillations of the cantilever is given by [17]

$$\frac{EI}{L^4} \frac{\partial^4 W(x,t)}{\partial x^4} + \mu \frac{\partial^2 W(x,t)}{\partial t^2} = F(x,t) + F_d(x,t), \quad (1)$$

where  $W(x,t)$  is the transverse displacement of the cantilever in the  $z$  direction as a function of its axial position  $x$  and time  $t$ . The axial position  $x$  is nondimensionalized with the cantilever length  $L$ . On the right hand side  $F$  is the force per unit length acting on the cantilever due to its interaction with the surrounding fluid and  $F_d$  is the force per unit length driving the cantilever motion. In our notation  $F_d$  is general and can be either an externally applied force or the Brownian force. For the remaining parameters,  $E$  is the Young's modulus,  $I$  is the area moment of inertia, and  $\mu$  is the mass per unit length of the cantilever. Since we are interested in solutions with dynamics oscillating in time, it is convenient to transform into Fourier space to yield,

$$\frac{EI}{L^4} \frac{\partial^4 \hat{W}(x,\omega)}{\partial x^4} + \mu \omega^2 \hat{W} = \hat{F}(x,\omega) + \hat{F}_d(x,\omega), \quad (2)$$

where  $\omega$  is the frequency of oscillation and we have used the transform convention,

$$\hat{W}(x,\omega) = \int_{-\infty}^{\infty} W(x,t) e^{i\omega t} dt, \quad (3)$$

$$W(x,t) = \frac{1}{2\pi} \int_{-\infty}^{\infty} \hat{W}(x,\omega) e^{-i\omega t} d\omega. \quad (4)$$

For the case of a cantilever beam of circular cross section oscillating in an unbounded fluid, the expression for the fluid force is [17,20,21],

$$\hat{F}_d(x,\omega) = \frac{\pi}{4} \rho_l \omega^2 b^2 \Gamma_c(\omega) \hat{W}(x,\omega), \quad (5)$$

where  $\rho_l$  is the density of the liquid and  $\Gamma_c$  is the hydrodynamic function for a circular cylinder. At large mode numbers, the hydrodynamic function depends on mode number [18,22]. However, for moderate mode number  $n \lesssim 3$  the hydrodynamic function for a circular cylinder is independent of mode number,

$$\Gamma_c(\omega) = 1 + \frac{4iK_1(-i\sqrt{i\text{Re}})}{\sqrt{i\text{Re}}K_0(-i\sqrt{i\text{Re}})} \quad (6)$$

where  $i$  is the usual imaginary unit,  $K_0$  and  $K_1$  are Bessel functions, and the subscript  $c$  is used to denote the result for a circular cylinder. The nondimensional parameter  $\text{Re}$  is the frequency parameter and plays the role of a frequency based Reynolds number,

$$\text{Re} = \frac{\omega b^2}{4\nu}, \quad (7)$$

where  $\nu$  is the kinematic viscosity of the fluid. The hydrodynamic force induced by an infinitely thin blade oscillating perpendicular to its face is well approximated by that of a circular cylinder of identical width; the maximum difference is of the order of 10% [23]. The hydrodynamic function for an oscillating flat blade can be expressed as,

$$\Gamma(\omega) = \Omega(\omega)\Gamma_c(\omega), \quad (8)$$

where the complex valued correction factor  $\Omega(\omega)$  is given explicitly in Ref. [17]. In all of our results we use the hydrodynamic function for a flat blade in Eq. (8).

We now construct an eigenfunction expansion,

$$\hat{W}(x, \omega) = \sum_{n=1}^{\infty} f_n(\omega) \phi_n(x), \quad (9)$$

where  $n$  is the mode number,  $f_n(\omega)$  is the frequency dependence of the  $n$ th mode, and  $\phi_n(x)$  is the normalized mode shape for the  $n$ th mode given by,

$$\begin{aligned} \phi_n(x) &= \cos(C_n x) - \cosh(C_n x) \\ &+ \frac{\cos(C_n) + \cosh(C_n)}{\sin(C_n) + \sinh(C_n)} [\sinh(C_n x) - \sin(C_n x)], \end{aligned} \quad (10)$$

where  $C_n$  is the  $n$ th root of,

$$1 + \cos C_n \cosh C_n = 0. \quad (11)$$

Inserting Eq. (9) into Eq. (5), using the orthogonality of the beam modes, and rearranging yields,

$$f_n(\omega) = \frac{L^4}{EI(C_n^4 - B(\omega)^4)} \int_0^1 \phi_n(x) \hat{F}_d(x, \omega) dx, \quad (12)$$

where

$$B(\omega) = C_1 \left( \frac{\omega}{\omega_1} \right)^{1/2} \left( 1 + \frac{\pi \rho_l b}{4 \rho_s h} \Gamma(\text{Re}) \right). \quad (13)$$

Therefore, given a particular driving force  $F_d(x, \omega)$  one has the desired solution using Eqs. (12) and (9).

#### A. Stochastic dynamics of a cantilever due to Brownian motion

For the case where the cantilever is driven by Brownian motion, we have

$$f_n(\omega) = \frac{L^3}{EI C_n^4 - B(\omega)^4} \hat{F}_{B,n}(\omega), \quad (14)$$

where

$$\hat{F}_{B,n}(\omega) = L \int_0^1 \phi_n(x) \tilde{F}_{B,n}(x, \omega) dx. \quad (15)$$

In our notation,  $\tilde{F}_{B,n}(x, \omega)$  is the Brownian force per unit length acting on the  $n$ th mode of the cantilever and  $\hat{F}_{B,n}(\omega)$  is

the total Brownian force acting on mode  $n$ . Inserting Eq. (14) into Eq. (9) yields,

$$\hat{W}(x, \omega) = \frac{L^3}{EI} \sum_{n=1}^{\infty} \frac{\phi_n(x) \hat{F}_{B,n}(\omega)}{C_n^4 - B(\omega)^4}. \quad (16)$$

The noise spectral density is then,

$$G_w(x, \omega) = |\hat{W}(x, \omega)|^2 = \left( \frac{L^3}{EI} \right)^2 \left| \sum_{n=1}^{\infty} \frac{\phi_n(x) \hat{F}_{B,n}(\omega)}{C_n^4 - B(\omega)^4} \right|^2. \quad (17)$$

From the fluctuation-dissipation theorem,

$$|\hat{F}_{B,n}(\omega)|^2 = 4k_B T \gamma_n(\omega), \quad (18)$$

where  $k_B$  is Boltzmann's constant,  $T$  is the temperature, and  $\gamma_n(\omega)$  is the total damping acting on mode  $n$ . For small mode number  $n \leq 3$  the damping is approximately mode independent to yield,

$$\gamma(\omega) = \frac{\pi}{4} \rho_l b^2 L \omega \Gamma_i(\omega), \quad (19)$$

where  $\Gamma_i$  is the imaginary part of  $\Gamma$  and  $\gamma(\omega)$  is the damping over the entire length of the cantilever. For larger mode number the hydrodynamic function becomes a function of  $n$  and this can be included if desired using the results of Ref. [18], which includes tabulated values for the hydrodynamic function. Using the above expression for the damping yields a noise spectral density given by,

$$G_w(x, \omega) = 4k_B T \left( \frac{L^3}{EI} \right)^2 \gamma(\omega) \left| \sum_{n=1}^{\infty} \frac{\phi_n(x)}{C_n^4 - B(\omega)^4} \right|^2, \quad (20)$$

and when evaluated at the cantilever tip yields,

$$G_w(x=1, \omega) = 16k_B T \left( \frac{L^3}{EI} \right)^2 \gamma(\omega) \left| \sum_{n=1}^{\infty} \frac{(-1)^n}{C_n^4 - B(\omega)^4} \right|^2, \quad (21)$$

where we have used  $\phi_n(1) = 2(-1)^n$  for all  $n$ . The noise spectral density for any single mode  $n$  is,

$$G_{n,w}(x, \omega) = 4k_B T \left( \frac{L^3}{EI} \right)^2 \gamma(\omega) \left| \frac{\phi_n(x)}{C_n^4 - B(\omega)^4} \right|^2, \quad (22)$$

and a physically more transparent expression can be found using Eqs. (13) and (19) to yield,

$$G_{n,w}(x, \omega) = \frac{k_B T}{k_n \omega_{0,n}} \frac{T_0 \tilde{\omega} \Gamma_i \phi_n^2(x)}{((1 - \tilde{\omega}^2(1 + T_0 \Gamma_r))^2 + (\tilde{\omega}^2 T_0 \Gamma_i)^2)}, \quad (23)$$

where  $\tilde{\omega} = \omega / \omega_{0,n}$  is the reduced frequency for the  $n$ th mode,  $\omega_{0,n}$  is the resonant frequency of the  $n$ th mode in vacuum,  $k_n$  is the dynamic spring constant of mode  $n$ , and  $\Gamma_r$  is the real part of  $\Gamma$ . The mass loading parameter

$$T_0 = \frac{\pi \rho_l b}{4 \rho_s h} \quad (24)$$

expresses the ratio of the mass of a cylinder of fluid with radius  $b/2$  to the mass of the cantilever.

In the limit of small displacements the angle of the cantilever  $\Theta(x, t)$  with respect to the horizontal is given by the axial derivative of  $W(x, t)$ . Therefore, the noise spectral density measured using the cantilever angle is,

$$G_{\theta}(x, \omega) = 4k_B T \left( \frac{L^3}{EI} \right)^2 \gamma(\omega) \left| \sum_{n=1}^{\infty} \frac{\phi'_n(x)}{C_n^4 - B(\omega)^4} \right|^2, \quad (25)$$

where  $\phi'_n(x)$  is the axial derivative of the mode shape. For a single mode  $n$ ,

$$G_{n,\theta}(x, \omega) = 4k_B T \left( \frac{L^3}{EI} \right)^2 \gamma(\omega) \left| \frac{\phi'_n(x)}{C_n^4 - B(\omega)^4} \right|^2, \quad (26)$$

which is equivalent to,

$$G_{n,\theta}(x, \omega) = \frac{k_B T}{k_n \omega_{0,n}} \frac{T_0 \tilde{\omega} \Gamma_i [\phi'_n(x)]^2}{\{[1 - \tilde{\omega}^2(1 + T_0 \Gamma_r)]^2 + (\tilde{\omega}^2 T_0 \Gamma_i)^2\}}. \quad (27)$$

We note that when evaluated at the tip,  $x=1$ , the noise spectral density based upon angle will have larger magnitudes for the higher modes because  $\phi'_n(1)/\phi_n(1)$  increases with  $n$  [6].

### B. Dynamics of a cantilever driven externally

We now consider the spectral properties of the cantilever oscillations when an external oscillating force is applied. From Eq. (12), it is clear that the spatial variation in the applied force is important. In order to connect directly with our experimental measurements using the spatially varying Lorentz force shown in Fig. 1(b) we consider an externally applied driving force of the form,

$$F_d(x, t) = \frac{F_0}{L} \begin{cases} \sin(\omega_d t) & x \leq \xi \\ 0 & x > \xi \end{cases}. \quad (28)$$

This corresponds to a sinusoidally time-varying and spatially uniform force applied over the region  $x \leq \xi$  where  $F_0$  is a constant force,  $\omega_d$  is the frequency of the driving force, and  $\xi$  is a nondimensional constant where:  $\xi=1$  corresponds to a uniform applied sinusoidal force over the entire length of the beam, and  $\xi=0$  corresponds to the absence of the applied force. In our calculations, this is a three-dimensional force applied to the entire bottom surface of the cantilever over the axial range given by  $\xi$ . Transforming into Fourier space yields,

$$f_n(\omega) = -i\pi \frac{L^3}{EI} \frac{1}{C_n^4 - B^4} (\delta(\omega + \omega_d) - \delta(\omega - \omega_d)) \int_0^{\xi} \phi_n(x) F(x) dx, \quad (29)$$

where  $\delta$  is the Dirac delta. Inserting Eq. (29) into Eq. (9) and solving for the power spectrum in terms of the cantilever displacement yields

$$P_w(x, \omega_d) = \left| \sum_{n=0}^{\infty} \hat{W}_n(x, \omega_d) \right|^2 = \left( \frac{\pi L^3 F_0}{EI} \right)^2 \left| \sum_{n=1}^{\infty} \frac{\phi_n(x) \int_0^{\xi} \phi_n(x) dx}{C_n^4 - B(\omega_d)^4} \right|^2, \quad (30)$$

and for any single mode, this simplifies to,

$$P_{n,w}(x, \omega_d) = \left( \frac{\pi F_0}{4k_n} \right)^2 \left[ \int_0^{\xi} \phi_n(x) dx \right]^2 \times \frac{\phi_n^2(x)}{\{[1 - \tilde{\omega}_d^2(1 + T_0 \Gamma_r)]^2 + (\tilde{\omega}_d^2 T_0 \Gamma_i)^2\}}. \quad (31)$$

In an experiment, one would sweep over  $\omega_d$  to generate the desired amplitude-frequency curve. In light of this and for simplicity of notation, we use  $\omega = \omega_d$  in the following expressions. Again, in the limit of small displacement, the power spectrum in terms of angle is given by the axial derivative to yield,

$$P_{\theta}(x, \omega) = \left( \frac{\pi L^3 F_0}{EI} \right)^2 \left| \sum_{n=1}^{\infty} \frac{\phi'_n(x) \int_0^{\xi} \phi_n(x) dx}{C_n^4 - B(\omega)^4} \right|^2, \quad (32)$$

and for any single mode, this yields,

$$P_{n,\theta}(x, \omega) = \left( \frac{\pi F_0}{4k_n} \right)^2 \left[ \int_0^{\xi} \phi_n(x) dx \right]^2 \times \frac{[\phi'_n(x)]^2}{\{[1 - \tilde{\omega}^2(1 + T_0 \Gamma_r)]^2 + (\tilde{\omega}^2 T_0 \Gamma_i)^2\}}. \quad (33)$$

There are a few points to make about these expressions for the power spectrum when evaluated for the dynamics of the cantilever tip. Since  $|\phi'_n(1)| > |\phi_n(1)|$ , the measurements in terms of angle will have larger relative values of the spectra peaks for the higher modes than what would be found for displacement measurements [6]. Also, the integral involving  $\xi$  will affect the relative magnitude of the spectral peaks.

The coefficients modifying the relative magnitude of the spectral peaks for the higher modes are different when the driving force is only applied to the cantilever tip. For this case,

$$F_d(x, t) = F_0 \sin(\omega_d t) \delta(x - 1), \quad (34)$$

where the force impulse is applied at the cantilever tip. The power spectrum in terms of cantilever displacement is,

$$P_w(x, \omega) = \left( \frac{4\pi F_0 L^3}{EI} \right)^2 \left| \sum_{n=1}^{\infty} \frac{\phi_n(1) \phi_n(x)}{C_n^4 - B(\omega)^4} \right|^2. \quad (35)$$

When evaluated at the cantilever tip this yields,

$$P_w(x=1, \omega) = \left( \frac{8\pi F_0 L^3}{EI} \right)^2 \left| \sum_{n=1}^{\infty} \frac{1}{C_n^4 - B(\omega)^4} \right|^2. \quad (36)$$

For any single mode  $n$ , this can be written as,

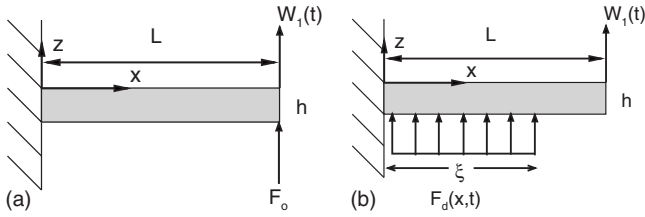


FIG. 2. A schematic of the forces used in the deterministic calculations to compute the noise spectral density  $G(\omega)$  and power spectrum  $P(\omega)$  of a cantilever of length  $L$ , width  $b$ , and height  $h$ . The deterministic displacement of the cantilever tip is given by  $W_1$ . (a) The removal of a step force  $F_0$  applied to the cantilever tip is used to determine the noise spectral density. (b) A spatially varying force impulse is used to numerically compute the power spectrum of flexural oscillations.

$$P_{n,w}(x, \omega) = \left( \frac{\pi F_0}{2k_n} \right)^2 \frac{\phi_n(1)\phi_n(x)}{((1 - \bar{\omega}^2(1 + T_0\Gamma_r))^2 + (\bar{\omega}^2 T_0\Gamma_i)^2)} \quad (37)$$

and when evaluated at the cantilever tip,

$$P_{n,w}(x=1, \omega) = \left( \frac{\pi F_0}{k_n} \right)^2 \frac{1}{((1 - \bar{\omega}^2(1 + T_0\Gamma_r))^2 + (\bar{\omega}^2 T_0\Gamma_i)^2)}. \quad (38)$$

The corresponding expression for  $P_\theta(x, \omega)$  is given by the axial derivative of Eq. (35). However, the slope of the mode shapes at the cantilever tip are a function of  $n$  and therefore do not yield a simple reduced expression in this case.

### III. NUMERICAL APPROACH

#### A. Stochastic dynamics—Fluctuation-dissipation theorem (step response)

The stochastic dynamics of cantilevers in a viscous fluid can be calculated from deterministic numerical simulations using linear response theory and the fluctuation-dissipation theorem [7,19]. The theoretical approach used is quite general, only the necessary details are included here and the reader is referred to Ref. [19] for a detailed discussion. The cantilever is released from a prescribed excursion from equilibrium and using linear response theory this is directly related to the autocorrelation in equilibrium fluctuations. The approach is general and can be used to compute the stochastic dynamics of any variable as long as the applied perturbation is conjugate to the dynamical variable of interest. The approach was originally used to compute the stochastic dynamics of cantilever displacement by calculating the cantilever ring down due to the removal of step force [7]. A point force is applied to the cantilever tip in the distant past and removed at time  $t=0$ ,

$$F_d(\mathbf{x}^*, t) = \begin{cases} F_0 & t \leq 0 \\ 0 & t > 0 \end{cases}, \quad (39)$$

where  $\mathbf{x}^*=(L, b/2, h/2)$  are the coordinates where the tip force is applied as shown in Fig. 2(a). The deterministic ring-

down of the cantilever tip displacement  $W_1(t)$  is related to the autocorrelation in equilibrium fluctuations in cantilever displacement by,

$$\langle w_1(0)w_1(t) \rangle = k_B T \frac{W_1(t)}{F_0}, \quad (40)$$

where  $w_1(t)$  is the stochastic displacement of the cantilever tip and the noise spectral density is given by,

$$G_w(\omega) = 4 \int_0^\infty \langle w_1(0)w_1(t) \rangle dt. \quad (41)$$

More recently, this approach was used to compute the dynamics in terms of the experimentally important quantity of cantilever angle [6]. In this case, a step point-torque is applied to the cantilever tip,

$$\tau_d(\mathbf{x}^*, t) = \begin{cases} \tau_0 & t \leq 0 \\ 0 & t > 0 \end{cases} \quad (42)$$

and the deterministic ring-down of the cantilever tip angle  $\Theta_1(t)$  is related to the autocorrelation in equilibrium fluctuations in cantilever angle by,

$$\langle \theta_1(0)\theta_1(t) \rangle = k_B T \frac{\Theta_1(t)}{\tau_0}, \quad (43)$$

where  $\theta_1(t)$  is the stochastic angle of the cantilever tip with respect to the horizontal. The noise spectral density is,

$$G_\theta(\omega) = 4 \int_0^\infty \langle \theta_1(0)\theta_1(t) \rangle dt. \quad (44)$$

We emphasize that in our notation the upper case  $W_1(t)$  and  $\Theta_1(t)$  indicate the deterministic motion of the cantilever tip as it rings down and the lower case  $w_1(t)$  and  $\theta_1(t)$  indicate the stochastic motion of the cantilever tip due to thermal motion.

#### B. Driven dynamics—transfer function (impulse response)

In order to calculate the cantilever dynamics due to an external driving force, we compute the cantilever's response to an appropriately chosen impulse in force. This has been done using an impulse in velocity to explore the driven dynamics of cantilevers beams of varying geometry, near a solid wall, and including the effects of higher modes of oscillation [24]. In what follows, we focus upon the dynamics of the fundamental flexural mode and allow the driving force to vary spatially given by,

$$F_d(\mathbf{x}^*, t) = \begin{cases} F_0 \delta(t) & x \leq \xi \\ 0 & x > \xi \end{cases}, \quad (45)$$

where again  $\mathbf{x}^*=(L, b/2, h/2)$  indicates the tip coordinates where the force is applied as shown in Fig. 2(b) where  $F_0$  is a constant force. The time dependent displacement of the cantilever  $W(x, t)$  due to the application of the drive force is computed numerically. The power spectrum in terms of cantilever displacement is then given by

TABLE I. Properties of the rectangular (1) and V-shaped (2) cantilevers shown in Fig. 1. The rectangular cantilever is the C2 cantilever of Ref. [17]. The V-shaped cantilever is an Olympus OMCL-TR400PSA lever. Given are the length  $L$ , width  $b$ , height  $h$ , spring constant  $k$ , torsional spring constant  $k_t$ , and the resonant frequency in vacuum  $f_0$ . For the V-shaped cantilever, the distance between the two arms at the base is  $b_1 = 106 \mu\text{m}$  and the distance from the base to the paddle region is  $L_1 = 40 \mu\text{m}$ . The values of  $k$ ,  $k_t$ , and  $f_0$  have been computed from finite element numerical simulations. Both cantilevers are mostly composed of silicon nitride, the rectangular cantilever has a Young's modulus  $E = 174 \text{ GPa}$  and a density  $\rho_c = 2320 \text{ kg/m}^3$  and for the V-shaped cantilever  $E = 172 \text{ GPa}$  and  $\rho_c = 2329 \text{ kg/m}^3$ . The cantilevers are placed in room temperature water with temperature  $T = 298 \text{ K}$ , density  $\rho_l = 997 \text{ kg/m}^3$ , and dynamic viscosity  $\eta = 8.59 \times 10^{-4} \text{ kg/m-s}$ .

Cantilever	$L$ ( $\mu\text{m}$ )	$b$ ( $\mu\text{m}$ )	$h$ ( $\mu\text{m}$ )	$k$ (N/m)	$k_t$ (N-m/rad)	$f_0$ (kHz)
(1)	197	29	2	1.3	$1.6 \times 10^{-8}$	71
(2)	100	13.4	0.4	0.08	$2.5 \times 10^{-10}$	32

$$P_w(x, \omega) = |\hat{W}(x, \omega)|^2. \quad (46)$$

The power spectrum in terms of cantilever angle is found by computing the slope of  $W(x, t)$  at the region of interest to yield  $\Theta(x, t)$  and

$$P_\theta(x, \omega) = |\hat{\Theta}(x, \omega)|^2. \quad (47)$$

An advantage of this approach is that the complete spectral response over all frequency, and for all modes, is determined from a single numerical simulation. The alternative of performing many simulations at different frequencies is computationally prohibitive for these systems.

It is interesting to point out a convenient simplification for the special case of an external actuation force applied to the cantilever tip only. For this situation, the power spectrum of cantilever oscillations can be found by applying a force impulse to the cantilever tip using the approach described above. However, in this case, the dynamics of the cantilever due to the removal of a step force applied to the tip is captured by the imaginary part of the cantilever response to the impulse [cf. Eq. (20) of Ref. [19]]. Therefore, for this case, both the power spectrum and noise spectral density are con-

veniently found from a single deterministic calculation, the response to a force impulse applied to the cantilever tip.

## IV. DISCUSSION

### A. Rectangular cantilever: Comparison of analytics with numerics

We first quantify the driven and stochastic dynamics of the rectangular cantilever described in Fig. 1(a) and Table I. A comparison of the noise spectral density and power spectrum are shown in Fig. 3 where the solid lines are from full numerical simulations and the dashed lines are analytical predictions. The spectra have been normalized by their maximum values and the frequency is plotted relative to the resonant frequency of the fundamental mode in vacuum. The noise spectral densities are shown in panel (a) and the power spectra are shown in panel (b). These results are for measurements based upon the angle of the cantilever tip.

The analytical prediction of the noise spectral density is given by Eq. (25) and the numerical results are computed using the torque-angle formulation discussed in Sec. III A. For the power spectrum, we have assumed a spatially uni-

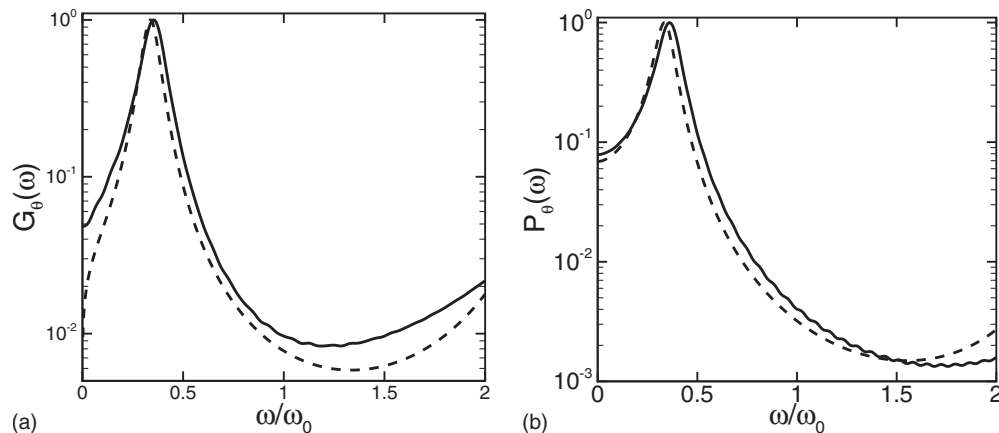


FIG. 3. A comparison of the computed noise spectral density and power spectrum with analytical predictions for the rectangular cantilever. (a) The variation in the noise spectra  $G_\theta(x=1, \omega)$  with frequency. (b) The variation in the power spectra  $P_\theta(x=1, \omega)$  with frequency for the case of a spatially uniform driving force  $\xi = 1$ . In both panels, the solid lines are results from numerical simulations and the dashed lines are analytical predictions. The spectra have been normalized by their maximum values.

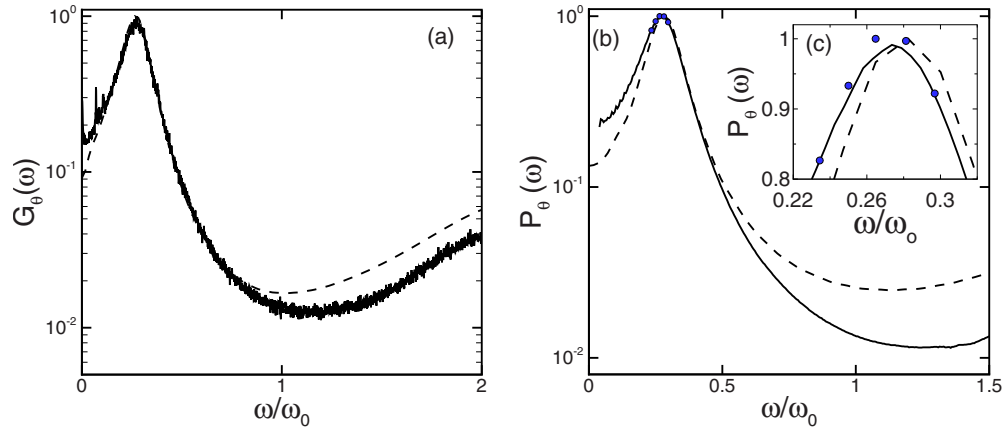


FIG. 4. (Color online) A comparison of the computed power spectra and noise spectral densities with experimental measurements using the V-shaped cantilever. (a) The variation in the noise spectral density  $G_\theta(x=1, \omega)$  with frequency where the solid line represents experimental measurements and the dashed line are results from finite element numerical simulations. (b) The variation in the power spectra  $P_\theta(x=1, \omega)$  with frequency. The solid line are results from experimental measurements and the dashed line is from numerical simulations. The simulations were conducted using a force impulse corresponding to the iDrive magnetomotive actuation. The blue circles are results from long-time numerical simulations conducted at five different frequencies. (c) A closer view of the peak to allow a better comparison of the experimental and numerical results.

form driving force that varies sinusoidally in time, which is given by Eq. (28) where  $\xi=1$ . The analytical results are found using Eq. (33) and the numerical results are computed from the cantilever response to an impulse in force as discussed in Sec. III B. Overall, the agreement is very good between the numerical and analytical results.

All of our deterministic computations are performed using transient three-dimensional finite element numerical simulations [25] for the fluid-solid interaction problem that describes the motion of the cantilever in a viscous fluid. We have performed extensive spatial and time resolution tests to ensure the accuracy of our numerical results. We have chosen the time step and spatial discretization in order to accurately compute the first resonance in fluid while incurring a reasonable computational overhead. For these simulations, we used  $250 \times 10^3$  elements with a uniform rectangular geometry having an average side length of approximately  $\Delta x \approx 1.5 \mu\text{m}$  and the time step was chosen to be  $\Delta t = 0.2 \mu\text{s}$ . It is useful to relate these values to properties of the beam in vacuum to provide some insight into how to estimate these values beforehand. The spatial resolution must be chosen to effectively resolve the frequency dependent viscous boundary layer that surrounds the cantilever. An estimate of the required spatial discretization is  $\Delta x \approx \delta_s$  where  $\delta_s = \sqrt{\nu/\omega_0}$  is the value of the Stokes length when measured using the resonant frequency in vacuum. For temporal discretization, we have found that  $\sim 70$  time steps per period of oscillation of the cantilever in vacuum is sufficient. In addition, care was taken to ensure that the bounding no-slip side walls of the computational domain were sufficiently distant so as to not affect the results significantly. The nearest side wall from the cantilever tip for these simulations was  $30 \mu\text{m}$ .

The deviations between the numerical and analytical results for frequencies smaller and larger than the fundamental resonance in fluid are due to limitations in the computations. At low frequency, the numerical results are limited by the finite simulation time used to compute the cantilever ring

down and the finite precision with which it is computed. At large frequencies, the computational results are most limited by spatial resolution constraints. The thickness of the viscous boundary layer that surrounds an oscillating object in fluid decreases with the inverse square root of the oscillation frequency. This leads to a dramatic increase in the required spatial resolution to compute the fluid-solid interactions at large frequencies.

### B. V-shaped Cantilever: Comparison of numerics with experiment

We now quantify the dynamics of a V-shaped micron scale cantilever that is used in the iDrive measurements. A schematic of the cantilever is shown in Fig. 1(b) and it is described further in Table I. Figure 4 illustrates a comparison between numerical and experimental results for the noise spectral density and the power spectrum. The numerical results for the noise spectral density are found using finite element simulations and the torque-angle formulation. The numerical results for the power spectrum are found using a force impulse corresponding to the magnetomotive actuation. This is accomplished by applying a distributed force with magnitude proportional to the angle of the wire in the applied magnetic field. Such a force distribution is similar to the uniform distribution employed in our analytic derivation, Eq. (28), and corresponds to an equivalent  $\xi \approx 0.5$ . Our model of the iDrive is approximate; we do not solve for the current flow to generate the Lorentz force. It is possible that better agreement would be achieved using a different value of  $\xi$ . However, we have not explored this in detail. For the calculations, we used  $260 \times 10^3$  elements of rectangular geometry with a typical side length  $\Delta x \approx 2 \mu\text{m}$  and a numerical time step  $\Delta t = 0.4 \mu\text{s}$ . In addition, the nearest bounding no-slip sidewall to the tip of the cantilever was at a distance of  $60 \mu\text{m}$ .

In order to validate our numerical approach for the calculation of the power spectrum using the impulse in force, we

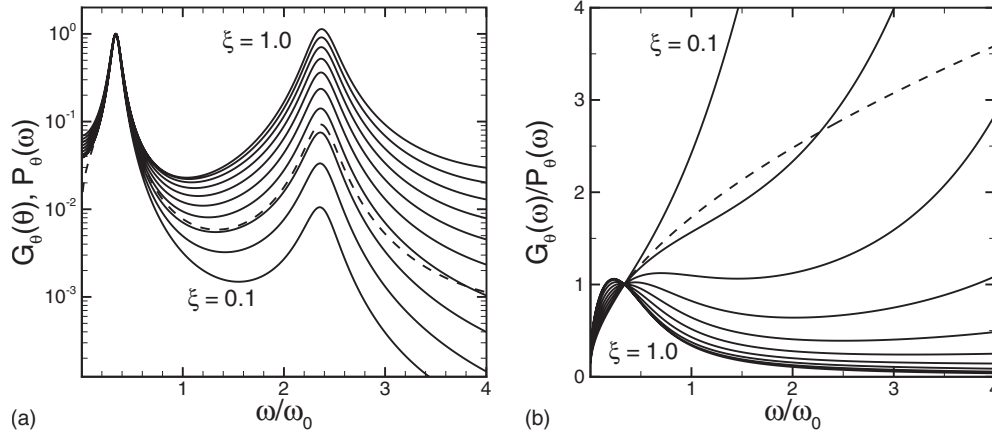


FIG. 5. Analytical predictions of the noise spectral density  $G_\theta(x=1, \omega)$  and power spectrum  $P_\theta(x=1, \omega)$  for the rectangular cantilever. (a) The noise spectral density is shown by the dashed line. The solid lines are the variation in the power spectrum with  $\xi$ . The bounding values of  $\xi$  are labeled and the subsequent curves are given in increments of 0.1. (b) The ratio of the noise spectral density to the power spectrum. The dashed line is the ratio using only the fundamental mode of vibration  $G_{1,\theta}(\omega)/P_{1,\theta}(\omega)$ . The solid lines are the ratio using the full solution  $G_\theta(\omega)/P_\theta(\omega)$  as a function of  $\xi$  using the same convention as panel (a).

performed the following test. We computed five separate long-time and fixed-frequency finite element numerical simulations to compute the power spectrum near the fundamental resonance. These results are shown in Figs. 4(b) and 4(c). The circles are results from the fixed frequency simulations, the dashed line is from simulations using an impulse in force, and the solid line is from experimental measurement. Overall, the agreement between the two numerical approaches is very good validating our approach using an impulse in force.

**C. Spectral properties of the power and noise spectra**

The relative magnitudes of the peaks of the power spectra depend upon the spatial variation in the external force that is applied. This is shown in Fig. 5(a) for the first two modes using analytical predictions for the rectangular cantilever. The noise spectral density  $G_\theta(x=1, \omega)$  is shown as the dashed line. The variation in the power spectra  $P_\theta(x=1, \omega)$  with  $\xi$  are shown by the solid lines for  $0.1 \leq \xi \leq 1$  in increments of 0.1. Figure 5(a) indicates that as  $\xi$  is increased the relative magnitude of the higher mode peaks increase.

In fact, at a value of  $\xi \approx 0.3$  the noise spectral density and power spectrum are nearly equal over a broad range in frequency. This is shown more clearly in Fig. 5(b) where the ratio  $G_\theta(\omega)/P_\theta(\omega)$  is plotted. The solid line is the variation in  $G_\theta(\omega)/P_\theta(\omega)$  with frequency as a function of  $\xi$  using the same convention as in panel (a). The dashed line is the ratio using only the fundamental mode  $G_{1,\theta}(\omega)/P_{1,\theta}(\omega)$ , which yields precisely the predicted frequency dependence of the damping  $\gamma(\omega)$  as given by Eq. (19). However, due to contributions from the higher modes, the frequency dependence of  $G_\theta(\omega)/P_\theta(\omega)$  is quite different. For  $\xi \approx 0.3$  the ratio is nearly constant at unity for  $0.5 \leq \omega/\omega_0 \leq 3$ .

Figure 6 shows a comparison of numerical and experimental results for the ratio of  $G_\theta(\omega)/P_\theta(\omega)$  for the V-shaped cantilever. The solid line are results from experiment and the dashed line are numerical results using the model of iDrive

actuation with equivalent  $\xi=0.5$ . The ratio of the spectra is nearly unity as predicted for a range of frequencies near the fundamental resonance indicating the similarity of the power and noise spectra for these conditions.

The frequency variation in the power spectra is quite different when the driving force is applied only at the cantilever tip. We have quantified this in Fig. 7 for the rectangular cantilever in terms of measurements of the cantilever angle at the tip. Figure 7(a) illustrates the power spectrum and noise spectrum. The solid lines are analytical predictions using Eq. (25) for the noise spectral density and the axial derivative of Eq. (35) for the power spectrum. The dashed lines are results from numerical simulations. For the power spectrum calculation, we have applied a force impulse at the cantilever tip. The agreement between the analytical and numerical spectra are quite good.

Figure 7(b) illustrates the ratio of the noise spectral density to the power spectrum. The dashed line is the ratio using only the spectra for the fundamental mode of oscillation. The

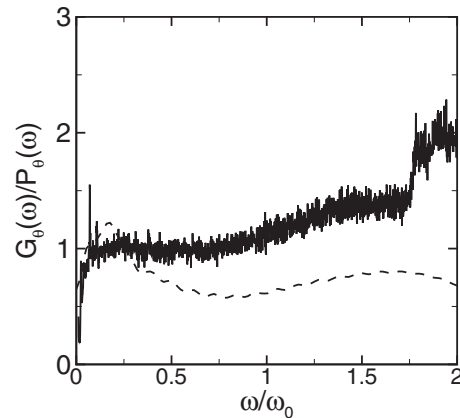


FIG. 6. The ratio of the noise spectral density  $G_\theta(x=1, \omega)$  to the power spectrum  $P_\theta(x=1, \omega)$  for the V-shaped cantilever using magnetic actuation. The solid line is from experiment and the dashed line are numerical results using finite element simulations.

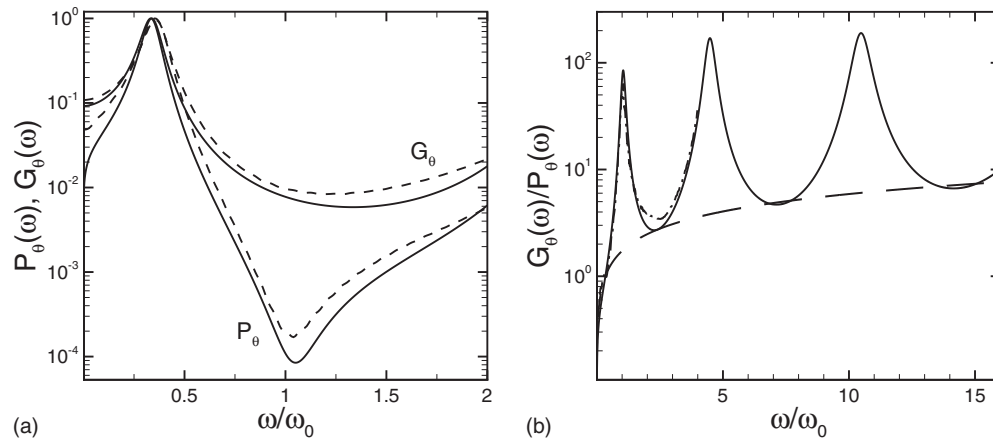


FIG. 7. (a) Using only sinusoidal tip-loading, the frequency variation in the noise spectral density  $G_\theta(x=1, \omega)$  and power spectrum  $P_\theta(x=1, \omega)$  of the rectangular cantilever. The frequency is normalized with the resonant frequency of the fundamental mode in vacuum  $\omega_0$ . The solid lines are analytical predictions and the dashed lines are from numerical simulations. (b) The ratio  $G_\theta(\omega)/P_\theta(\omega)$  where the solid line is the analytical prediction, the dash-dotted line is the result from numerical simulation, and the dashed line is the analytical prediction using only a single mode. The numerical results are only shown for  $\omega/\omega_0 \lesssim 4$  since higher frequencies are not resolved using the chosen simulation parameters.

solid line represents analytical predictions and the dash-dotted line are the results from numerical simulation. The frequency range of the plot is quite large to include the contributions from several modes of oscillation. The numerical results are only shown for  $\omega/\omega_0 \lesssim 4$ , which includes the range of frequency that is resolved by the parameters of the numerical simulations. Using our approach, to compute the contributions from the higher modes numerically requires a substantial increase in both the spatial and temporal resolution. The large spikes in the magnitude of the spectra ratio are due to the large difference in the magnitude of the spectra between the peaks of the individual modes. In these regions between the peaks, the contributions from the tails of the higher modes are most significant. As a result, the ratio of the spectra when including the contributions from only a single mode is significantly different.

## V. CONCLUSION

We have explored the spectral properties of oscillating micron scale cantilevers in a viscous fluid. The analytical expressions and the numerical approach discussed have a broad range of applicability that can be used to gain physical insights and guide future experiments. Despite the significant

physical differences between driving a cantilever externally or using only thermal motion, we have described a unified approach to quantify the dynamics that requires only straight forward deterministic calculations. Using these ideas, we have quantified the spectral properties of the cantilever for the precise conditions of experiment. Our results reveal a very strong dependence upon higher modes of oscillation and on the precise spatial variation in the external actuation. Surprisingly, there are interesting deviations from what one would expect using a naive single mode approximation, even for frequencies near the fundamental resonance. It is anticipated that our results will be useful in future theoretical studies as well as in the development of micro and nanoscale technologies that exploit the high frequency oscillations of elastic objects in viscous fluids.

## ACKNOWLEDGMENTS

M.R.P. and M.T.C. acknowledge funding by AFOSR under Grant No. FA9550-07-1-0222 and a Virginia Tech ASPIRES grant. J.E.S. acknowledges support from the Australian Research Council Grants Scheme. The authors thank S. Hohlbauch of Asylum Research for providing experimental data.

- [1] K. L. Ekinici and M. L. Roukes, *Rev. Sci. Instrum.* **76**, 061101 (2005).
- [2] A. Raman, J. Melcher, and R. Tung, *Nanotoday* **3**, 20 (2008).
- [3] R. García and R. Pérez, *Surf. Sci. Rep.* **47**, 197 (2002).
- [4] R. J. Clarke, S. M. Cox, P. M. Williams, and O. E. Jensen, *J. Fluid Mech.* **545**, 397 (2005).
- [5] C. P. Green and J. E. Sader, *Phys. Fluids* **17**, 073102 (2005).
- [6] M. T. Clark and M. R. Paul, *J. Appl. Phys.* **103**, 094910

(2008).

- [7] M. R. Paul and M. C. Cross, *Phys. Rev. Lett.* **92**, 235501 (2004).
- [8] M. T. Clark and M. R. Paul, *Int. J. Non-Linear Mech.* **42**, 690 (2007).
- [9] T. P. Burg, M. Godin, S. M. Knudsen, W. Shen, G. Carlson, J. S. Foster, K. Babcock, and S. R. Manalis, *Nature* **446**, 1066 (2007).

- [10] T. P. Burg, J. E. Sader, and S. R. Manalis, *Phys. Rev. Lett.* **102**, 228103 (2009).
- [11] The idrive magnetomotive actuation is available from Asylum Research, Santa Barbara, California 93117.
- [12] H.-J. Butt and M. Jaschke, *Nanotechnology* **6**, 1 (1995).
- [13] H. B. Callen and T. A. Welton, *Phys. Rev.* **83**, 34 (1951).
- [14] H. B. Callen and R. F. Greene, *Phys. Rev.* **86**, 702 (1952).
- [15] L. Onsager, *Science* **166**, 1359 (1969).
- [16] D. Chandler, *Introduction to Modern Statistical Mechanics* (Oxford University Press, New York, 1987).
- [17] J. E. Sader, *J. Appl. Phys.* **84**, 64 (1998).
- [18] C. A. van Eysden and J. E. Sader, *J. Appl. Phys.* **101**, 044908 (2007).
- [19] M. R. Paul, M. T. Clark, and M. C. Cross, *Nanotechnology* **17**, 4502 (2006).
- [20] G. G. Stokes, *Trans. Cambridge Philos. Soc.* **9**, 8 (1850).
- [21] L. Rosenhead, *Laminar Boundary Layers* (Oxford University Press, New York, 1963).
- [22] C. A. Van Eysden and J. E. Sader, *J. Appl. Phys.* **106**, 094904 (2009).
- [23] E. O. Tuck, *J. Eng. Math.* **3**, 29 (1969).
- [24] S. Basak, A. Raman, and S. V. Garimella, *J. Appl. Phys.* **99**, 114906 (2006).
- [25] ESI CFD Headquarters, Huntsville AL 25806. We use the CFD-ACE+ solver.